Progress In Electromagnetics Research, PIER 76, 141–152, 2007

INTEGRAL PML ABSORBING BOUNDARY CONDITIONS FOR THE HIGH-ORDER M24 FDTD ALGORITHM

A. M. Shreim and M. F. Hadi

Electrical Engineering
Kuwait University
P.O. Box 5969, Safat 13060, Kuwait

Abstract—This work demonstrates an efficient and simple PML absorbing boundary conditions (ABCs) implementation for the high-order extended-stencil M24 FDTD algorithm. To accomplish this objective, the integral forms of the PML split-field formulations were derived and discretized using the same M24 weighted multiple-loop approach, resulting in ABC performances that match the standard FDTD-based PML formulations. This proposed approach eliminates the impedance mismatches caused by switching from M24 to regular FDTD update equations within the PML regions and the necessary cumbersome subgridding implementations needed to minimize the effects of these mismatches. It also eliminates the need to use large separations between the scatterers and the PML regions as a simpler though more costly alternative. This achievement coupled with the recent effective resolution of the PEC modeling issue finally eliminates the last hurdles hindering the wide adoption of the M24 algorithm and its three-dimensional counterpart, the FV24 algorithm, as a viable option for accurate and computationally efficient modeling of electrically large structures.

1. INTRODUCTION

The perfectly-matched layer (PML) absorbing boundary condition (ABC) introduced by Bérenger in 1994 [1] proved to be as versatile and widely used as the FDTD method itself, for which it was designed, as evidenced by the many and varied extensions and specialized implementations in the literature [2–6]. Most of these works, however, catered to the FDTD method in its standard form (S_{22} for second-order finite differencing in both time and space of

Maxwell's equations). Consequently, the optimum PML parameters proposed by the various researches and invariably used in later PML applications as is (e.g., [7–10]) can only be relied upon for the S_{22} algorithm. In particular, only a few published works considered investigating PML parameter sensitivities and trade-offs when used in higher order FDTD implementations [11, 12]. The latter reference in particular demonstrated the clear advantage of custom-optimized PML parameters for high-order FDTD implementations, in that case Fang's standard fourth-order time and space finite-difference (or S_{44}) algorithm [13].

The highly phase-coherent M24 algorithm developed by Hadi and Piket-May [14], which is the subject of this work, differs from other high-order FDTD algorithms in that it relies strictly on the integral form of Maxwell's equations and thus cannot be implemented directly within the PML region with its differential form-based formulations. The workaround in [14] was to switch from M24 to S_{22} update equations as soon as the PML inner boundaries are encountered. This transition from one differencing scheme to another proved to be a major source of spurious reflections as demonstrated by Hadi and Dib [15], especially for waves impinging on the interface at steep angles. This phenomenon necessitates large and computationally costly separations between the scatterer and the PML layers to ensure that most outgoing energy will impinge on the boundaries at angles within the relatively tame range of ± 75 degrees. For the wave propagation through a building problem in [14] as an example, this meant an unwelcome increase of the total modeled domain size to $48\lambda \times 51\lambda$ even though the maximum building dimensions were $22\lambda \times 33\lambda$. That amounted to more than three-fold increase in both memory requirements and simulation times, just to accommodate the absorbing boundary conditions.

In this presented work the PML split-field formulations will be revisited and related to the integral forms of Maxwell's equations. The new forms will then be used to directly implement the M24 algorithm within the PML absorbing boundary conditions. Following that, comparative sensitivity analysis of the various PML parameters will be conducted for both M24 and the benchmark S_{22} algorithms to validate the new formulations.

2. INTEGRAL EQUIVALENCE OF THE PML SPLIT-FIELD DIFFERENTIAL EQUATIONS

Bérenger's PML ABCs are based on the idea of splitting the differential form of Maxwell's equations into twin sets of equations that would allow introducing independent PML loss profiles along the FDTD grid

axial dimensions. Considering as an example the two dimensional TM^z equations ($\partial/\partial z = 0$)

$$\epsilon\frac{\partial E_z}{\partial t} + \sigma E_z = \frac{\partial H_y}{\partial x} - \frac{\partial H_x}{\partial y} \quad (1)$$

$$\mu\frac{\partial H_x}{\partial t} + \sigma^* H_x = -\frac{\partial E_z}{\partial y} \quad (2)$$

$$\mu\frac{\partial H_y}{\partial t} + \sigma^* H_y = \frac{\partial E_z}{\partial x}, \quad (3)$$

we can write the Bérenger twin-equation version of (1)

$$\left\{ \begin{array}{c} \epsilon\dfrac{\partial E_{zx}}{\partial t} + \sigma_x E_{zx} \\ \epsilon\dfrac{\partial E_{zy}}{\partial t} + \sigma_y E_{zy} \end{array} \right\} = \left\{ \begin{array}{c} \dfrac{\partial H_y}{\partial x} \\ -\dfrac{\partial H_x}{\partial y} \end{array} \right\} \quad (4)$$

with $E_z = E_{zx} + E_{zy}$ in (2)–(3). These equations can be re-cast into their integral forms as

$$\left\{ \begin{array}{c} \int\left(\epsilon\dfrac{\partial E_{zx}}{\partial t} + \sigma_x E_{zx}\right)\cdot d\bar{s} \\ \int\left(\epsilon\dfrac{\partial E_{zy}}{\partial t} + \sigma_y E_{zy}\right)\cdot d\bar{s} \end{array} \right\} = \left\{ \begin{array}{c} \oint_{C_x} \bar{H}\cdot d\bar{\ell} \\ \oint_{C_y} \bar{H}\cdot d\bar{\ell} \end{array} \right\}, \quad (5)$$

where C_x and C_y are the same square $h \times h$ FDTD loop that circulates an E_z node in a standard staggered Yee cell, except that C_x includes only the H_y tangential nodes and C_y includes only the H_x tangential nodes as demonstrated in Fig. 1. Discretizing (5) according to these loop definitions will produce the same E_{zx} and E_{zy} update equations as those traditionally produced from (4)

$$E_{zx}|_{i,j}^{n+\frac{1}{2}} = e^{-\sigma_x\Delta t/\epsilon}E_{zx}|_{i,j}^{n-\frac{1}{2}} + \frac{1-e^{-\sigma_x\Delta t/\epsilon}}{\sigma_x h}\left(H_y|_{i+\frac{1}{2},j}^{n} - H_y|_{i-\frac{1}{2},j}^{n}\right) \quad (6)$$

$$E_{zy}|_{i,j}^{n+\frac{1}{2}} = e^{-\sigma_y\Delta t/\epsilon}E_{zy}|_{i,j}^{n-\frac{1}{2}} + \frac{1-e^{-\sigma_y\Delta t/\epsilon}}{\sigma_y h}\left(H_x|_{i,j-\frac{1}{2}}^{n} - H_x|_{i,j+\frac{1}{2}}^{n}\right). \quad (7)$$

The remaining two TM^z update equations are derived in a similar manner,

$$H_x|_{i,j}^{n+\frac{1}{2}} = e^{-\sigma_y^*\Delta t/\mu}H_x|_{i,j}^{n-\frac{1}{2}} + \frac{1-e^{-\sigma_y^*\Delta t/\mu}}{\sigma_y^* h}\left(E_z|_{i,j-\frac{1}{2}}^{n} - E_z|_{i,j+\frac{1}{2}}^{n}\right) \quad (8)$$

$$H_y|_{i,j}^{n+\frac{1}{2}} = e^{-\sigma_x^*\Delta t/\mu}H_y|_{i,j}^{n-\frac{1}{2}} + \frac{1-e^{-\sigma_x^*\Delta t/\mu}}{\sigma_x^* h}\left(E_z|_{i+\frac{1}{2},j}^{n} - E_z|_{i-\frac{1}{2},j}^{n}\right). \quad (9)$$

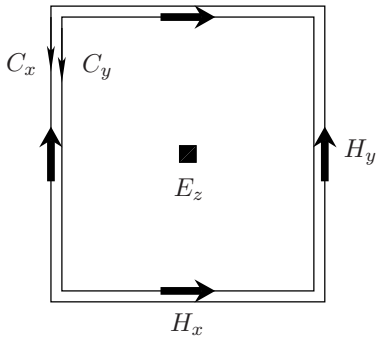

Figure 1. Ampere's law representation of the PML split $E_z = E_{zx} + E_{zy}$ update equation: C_x loop for E_{zx} and C_y loop for E_{zy}.

In these equations, Holland's exponential time-stepping formula [16] was used to model the PML loss profiles and the electric and magnetic conductivities are related by $\sigma/\epsilon = \sigma^*/\mu$ as mandated by the PML theory.

Using the loop integrals approach, however, is quite beneficial for the M24 algorithm since it is strictly based on Maxwell's integral equation forms. The M24 algorithm, it must be remembered, utilizes multiple weighted Ampere's and Faraday's loop integrals over extended-stencil FDTD cells as shown in Fig. 2, where the weighting coefficients K_a, K_b and K_c are tuning parameters that serve to minimize the effect of numerical dispersion on wave propagation within the discrete FDTD lattice. Dispersion analysis have shown [14] that for the S_{22} algorithm to match the phase accuracy of the M24 algorithm, it must use extremely fine resolution factors (R cells per wavelength) in the order of

$$R_{\text{S22}} = R_{\text{M24}}^3 \qquad \text{and} \qquad R_{\text{S22}} = R_{\text{M24}}^2 \tag{10}$$

for single-frequency and wideband applications, respectively.

3. EXTENDING THE M24 FORMULATION INTO THE PML REGIONS

Using the split-loop approach of (5) we can write the M24-style multiply-weighted formulas

$$\left[\epsilon\frac{\partial E_{zx}}{\partial t} + \sigma_x E_{zx}\right]_{\text{PML}} = K_a\left[\epsilon\frac{\partial E_{zx}}{\partial t} + \sigma_x E_{zx}\right]_{C_{ax}} + K_b\left[\epsilon\frac{\partial E_{zx}}{\partial t} + \sigma_x E_{zx}\right]_{C_{bx}} + K_c\left[\epsilon\frac{\partial E_{zx}}{\partial t} + \sigma_x E_{zx}\right]_{C_{cx}} \tag{11}$$

$$\left[\epsilon\frac{\partial E_{zy}}{\partial t}+\sigma_y E_{zy}\right]_{\mathrm{PML}} = K_a\left[\epsilon\frac{\partial E_{zy}}{\partial t}+\sigma_y E_{zy}\right]_{C_{ay}} + K_b\left[\epsilon\frac{\partial E_{zy}}{\partial t}+\sigma_y E_{zy}\right]_{C_{by}} + K_c\left[\epsilon\frac{\partial E_{zy}}{\partial t}+\sigma_x E_{zy}\right]_{C_{cy}} \quad (12)$$

which can be re-cast using Ampere's law and with the help of Fig. 3 into

$$\epsilon\frac{\partial E_{zx}}{\partial t}+\sigma_x E_{zx} = \frac{K_a}{h^2}\oint_{C_{ax}}\bar{H}\cdot d\bar{\ell}+\frac{K_b}{9h^2}\oint_{C_{bx}}\bar{H}\cdot d\bar{\ell}+\frac{K_c}{9h^2}\oint_{C_{cx}}\bar{H}\cdot d\bar{\ell} \quad (13)$$

$$\epsilon\frac{\partial E_{zy}}{\partial t}+\sigma_y E_{zy} = \frac{K_a}{h^2}\oint_{C_{ay}}\bar{H}\cdot d\bar{\ell}+\frac{K_b}{9h^2}\oint_{C_{by}}\bar{H}\cdot d\bar{\ell}+\frac{K_c}{9h^2}\oint_{C_{cy}}\bar{H}\cdot d\bar{\ell}. \quad (14)$$

The corresponding M24-PML update equations will now be

$$E_{zx}|_{i,j}^{n+\frac{1}{2}} = e^{-\sigma_x\Delta t/\epsilon}E_{zx}|_{i,j}^{n-\frac{1}{2}}+\frac{1-e^{-\sigma_x\Delta t/\epsilon}}{\sigma_x}\cdot \left\{\begin{array}{l} \dfrac{K_a}{h}\left(H_y|_{i+\frac{1}{2},j}^{n}-H_y|_{i-\frac{1}{2},j}^{n}\right) \\ +\dfrac{K_b}{3h}\left(H_y|_{i+\frac{3}{2},j}^{n}-H_y|_{i-\frac{3}{2},j}^{n}\right) \\ +\dfrac{K_c}{6h}\left(\begin{array}{c} H_y|_{i+\frac{3}{2},j-1}^{n}+H_y|_{i+\frac{3}{2},j+1}^{n} \\ -H_y|_{i-\frac{3}{2},j-1}^{n}-H_y|_{i-\frac{3}{2},j+1}^{n}\end{array}\right)\end{array}\right\} \quad (15)$$

$$E_{zy}|_{i,j}^{n+\frac{1}{2}} = e^{-\sigma_y\Delta t/\epsilon}E_{zy}|_{i,j}^{n-\frac{1}{2}}+\frac{1-e^{-\sigma_y\Delta t/\epsilon}}{\sigma_y}\cdot \left\{\begin{array}{l} \dfrac{K_a}{h}\left(H_x|_{i,j-\frac{1}{2}}^{n}-H_x|_{i,j+\frac{1}{2}}^{n}\right) \\ +\dfrac{K_b}{3h}\left(H_x|_{i,j-\frac{3}{2}}^{n}-H_x|_{i,j+\frac{3}{2}}^{n}\right) \\ +\dfrac{K_c}{6h}\left(\begin{array}{c} H_x|_{i-1,j-\frac{3}{2}}^{n}+H_x|_{i+1,j-\frac{3}{2}}^{n} \\ -H_x|_{i-1,j+\frac{3}{2}}^{n}-H_x|_{i+1,j+\frac{3}{2}}^{n}\end{array}\right)\end{array}\right\}. \quad (16)$$

The remaining two TM^z update equations are derived in a similar manner,

$$H_x|_{i,j}^{n+\frac{1}{2}} = e^{-\sigma_y^*\Delta t/\mu}H_x|_{i,j}^{n-\frac{1}{2}}+\frac{1-e^{-\sigma_y^*\Delta t/\mu}}{\sigma_y^*}\cdot$$

$$\left\{ \begin{array}{l} \dfrac{1-K_b}{h}\left(E_z|^n_{i,j-\frac{1}{2}} - E_z|^n_{i,j+\frac{1}{2}}\right) \\ +\dfrac{K_b}{3h}\left(E_z|^n_{i,j-\frac{3}{2}} - E_z|^n_{i,j+\frac{3}{2}}\right) \end{array} \right\} \tag{17}$$

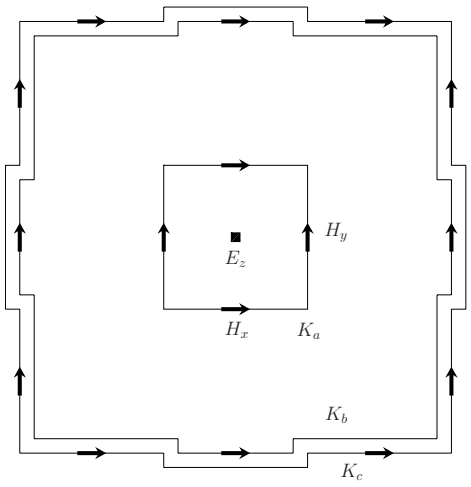

Figure 2. Multiple weighted Ampere's loops for updating a centered E_z node in the M24 algorithm. A uniform $\Delta x = \Delta y = h$ is assumed and $K_a = 1 - K_b - K_c$.

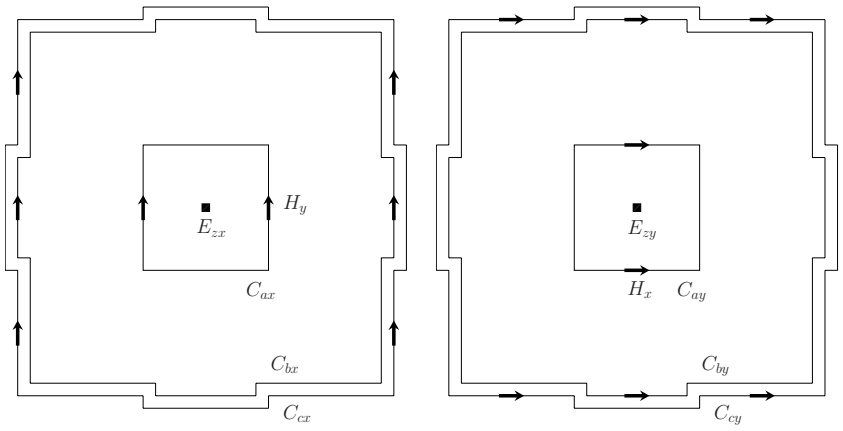

Figure 3. The split concentric Ampere's loops for the M24-PML cells. E_{zx} and E_{zy} occupy the same point in space. They are shifted for illustration purposes only.

Table 1. K_b and K_c values for the M24 algorithm which are applicable within the PML regions.

R	K_b	K_c
5	−0.144931711	0.1020689016
10	−0.116192765	0.0734445091
20	−0.110322272	0.0678920244
30	−0.109282656	0.0669204693

$$H_y|_{i,j}^{n+\frac{1}{2}} = e^{-\sigma_x^*\Delta t/\mu} H_y|_{i,j}^{n-\frac{1}{2}} + \frac{1-e^{-\sigma_x^*\Delta t/\mu}}{\sigma_x^*} \cdot \left\{ \begin{array}{l} \dfrac{1-K_b}{h}\left(E_z|_{i+\frac{1}{2},j}^{n} - E_z|_{i-\frac{1}{2},j}^{n}\right) \\ \\ +\dfrac{K_b}{3h}\left(E_z|_{i+\frac{3}{2},j}^{n} - E_z|_{i-\frac{3}{2},j}^{n}\right) \end{array} \right\}. \quad (18)$$

For simplicity, the K-parameters in the above equations are the same ones used for the scatterer region and the reader is referred to [14] for their calculation procedure.† Table 1 lists a few pre-calculated, frequency-independent values for several FDTD resolutions. As for the cells immediately adjacent to the PEC backplanes of the PMLs, the specialized phase -matched update equations developed in [15] could be used. If the M24-PML design parameters are properly chosen however, opting for the simpler S_{22} update equations there should cause no ill-effects. What remains now is to find appropriate PML parameters that best fit the M24 algorithm which may not necessarily coincide with those favorable to the S_{22} algorithm.

4. OPTIMUM M24-PML DESIGN PARAMETERS

The main PML parameters that need to be optimized for M24 algorithm implementations are the PML depth, d, the conductivity profile order, n (polynomial profiles are assumed), and the target

† Thankfully, optimizing numerical isotropy is unnecessary within the PML regions. Otherwise, the lossy version of the dispersion relation there would have needed to be derived and used to calculate specific optimized K-parameters for each incremental PML depth.

theoretical reflection coefficient normal to the scatterer-PML interface, $R(0)$. All these parameters are interlinked through [1]

$$\sigma(\rho) = \sigma_{\max} \left(\frac{\rho}{d}\right)^n \tag{19}$$

and

$$R(0) = \exp\left[-\frac{2}{n+1}\frac{\sigma_{\max} d}{\epsilon c}\right], \tag{20}$$

where ρ is the incremental depth of the PML layer starting at the scatterer-PML interface and c is the vacuum wave velocity.

Following the example of Taflove [17], an experimental setup is implemented to test the proposed M24-PML formulation where a point source pulse is initiated at the center of an empty 100 by 50-cells-large scatterer region surrounded by the absorbing boundary under test. The same test parameters and observation procedure as in [17] are followed and need not be repeated here. The only exception being that an averaged normalized spurious reflection coefficients are calculated from the entire length of the scatterer-PML bottom interface at one cell away into the scatterer region and used as a comparison figure of merit.

Fig. 4a demonstrates the clear advantage of the M24-PML formulation presented in this work evidenced by a local spurious reflections reduction of approximately 35 dB off the PML ABC, compared to the hybrid scheme that uses M24 formulation for the scatterer region and S_{22} for the PML regions. Furthermore, Fig. 4b shows the excellent match between the spurious reflections levels of the proposed M24-PML formulation and the standard S_{22}-PML formulation.

Fig. 5 illustrates the spurious reflections, averaged across the bottom scatterer/PML interface, at several selections of PML depths (d), target theoretical normal reflections ($R(0)$), and conductivity profiles (n). Several observations can be made from these comparative plots:

(i) In most combinations of d, $R(0)$ and n, a close match is achieved between the M24-PML and S_{22}-PML performances. The only exception being with the cubic conductivity profile ($n = 3$), where the M24-PML formulation exhibits a slightly inferior performance compared to that of the S_{22}-PML. A possible explanations is the inability of the extended-stencil M24 cells from closely tracking the fast changing conductivity values from one incremental PML depth to the next at such a steep profile.

(ii) Both formulations show limited sensitivities to the $R(0)$ parameter as long as the chosen value is within the range 10^{-6} to 10^{-8}.

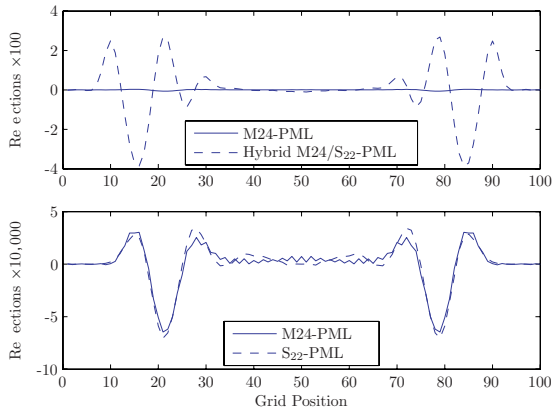

Figure 4. Comparing the normalized spurious reflections off the PML interface for the M24-PML, S_{22}-PML and the hybrid M24 in the scatterer region/S_{22} in the PML region. PML parameters used: 15-cell depth, $R(0) = 10^{-7}$ and parabolic ($n = 2$) conductivity profile.

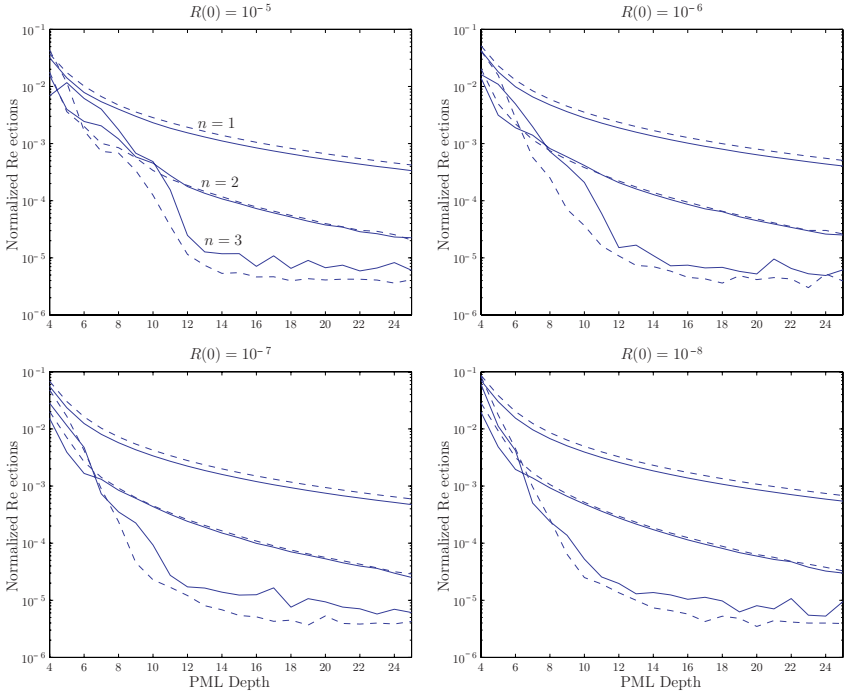

Figure 5. PML design curves for the M24-PML (solid) and S_{22}-PML (dashed) algorithms at several values of $R(0)$, conductivity profile order n and PML depth (number of cells).

(iii) The optimum M24-PML parameters are $d = 12$ to 15 cells, and $n = 3$ (cubic conductivity profile).

(iv) For shallow M24-PML depths (under 6 cells deep), a parabolic ($n = 2$) conductivity profile will out-perform the cubic profile. Since the M24 algorithm is meant for modeling electrically large structures however, choosing the larger optimum PML depths above will only add a small percentage to the computational cost of the model.

(v) Further analysis have shown that increasing the PML conductivity profile order beyond $n = 3$ has limited or no added advantage for either algorithm as illustrated in Fig. 6.

In all the above analysis a consistent FDTD grid resolution of $R = 20$ cells per wavelength was used.

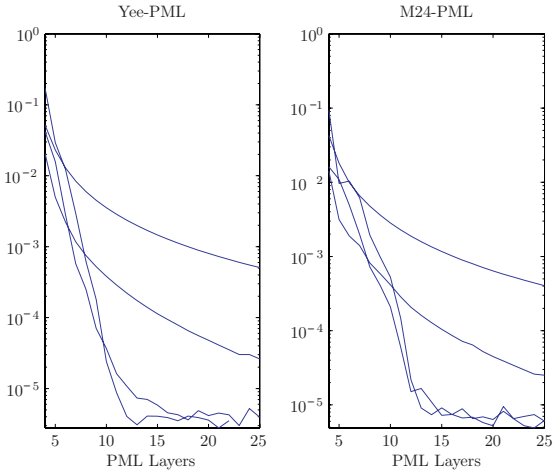

Figure 6. Comparison of spurious reflections for S_{22}-PML and M24-PML implementations. In each plot the four curves correspond to (from top to bottom at 13 layers) $n = 1, 2, 3, 4$. $R(0) = 10^{-6}$.

5. CONCLUSION

Although extended-stencil high-order algorithms such as the M24 formulation have consistently demonstrated superior phase accuracy, they have long been suffering from neglect due to their inherent modeling challenges around PEC and ABC boundaries. The PEC modeling issue has been recently resolved in an efficient and simple manner for the M24 algorithm, and the successful formulation was later extended to its 3D version, the FV24 algorithm [18]. In this present

work, the remaining challenge of absorbing boundary conditions has also been solved in an efficient and simple manner. Through recasting the Bérenger split-field formulations into their integral forms, the same multiple loop formulations of the M24 algorithm were made possible within the PML regions. This successful realization removed the highly disruptive stipulation of having to stop the M24 update equations short of the PML regions and switching to the lower order FDTD update equations with the inevitable cross-scheme impedance mismatches. With such effective resolutions to the PEC and ABC modeling issues, the highly phase-coherent M24 (and FV24) algorithm can now be used exclusively throughout the computational domain. Both developed PEC and ABC solutions can also be easily adapted to other extended-stencil high-order FDTD algorithms.

REFERENCES

1. Bérenger, J.-P., "A perfectly matched layer for the absorption of electromagnetic waves," *Journal of Computational Physics*, Vol. 114, No. 2, 185–200, 1994.
2. Chew, W. C. and W. H. Weedon, "A 3D perfectly matched medium from modified Maxwell's equations with stretched coordinates," *Microwave Opt. Technol. Lett.*, Vol. 7, No. 13, 599–604, Sept. 1994.
3. Bérenger, J.-P., "An effective PML for the absorption of evanescent waves in waveguides," *IEEE Microwave Guided Wave Lett.*, Vol. 8, No. 5, 188–190, May 1998.
4. Sacks, Z. S., D. M. Kingsland, R. Lee, and J. F. Lee, "A perfectly matched anisotropic absorber for use as an absorbing boundary condition," *IEEE Trans. Antennas Propagat.*, Vol. 43, No. 12, 1460–1463, Dec. 1995.
5. Roden, J. A. and S. D. Gedney, "Convolution PML (CPML): An efficient FDTD implementation of the CFS-PML for arbitrary media," *Microwave Opt. Technol. Lett.*, Vol. 27, No. 5, 334–339, Dec. 2000.
6. Shi, Y. and C.-H. Liang, "A strongly well-posed pml with unsplit-field formulations in cylindrical and spherical coordinates," *Journal of Electromagnetic Waves and Applications*, Vol. 19, No. 13, 1761–1776, 2005.
7. Uduwawala, D., M. Norgren, P. Fuks, and A. Gunawardena, "A complete fdtd simulation of a real gpr antenna system operating above lossy and dispersive grounds," *Progress In Electromagnetics Research*, PIER 50, 209–229, 2005.

8. Ali, M. and S. Sanyal, "FDTD analysis of dipole antenna as EMI sensor," *Progress In Electromagnetics Research*, PIER 69, 341–359, 2007.
9. Chen, X., D. Liang, and K. Huang, "Microwave imaging 3-d buried objects using parallel genetic algorithm combined with fdtd technique," *Journal of Electromagnetic Waves and Applications*, Vol. 20, No. 13, 1761–1774, 2006.
10. Golestani-Rad, L., J. Rashad-Mohassel, and M.-M. Danaie, "Rigorous analysis of em-wave penetration into a typical room using fdtd method: The transfer function concept," *Journal of Electromagnetic Waves and Applications*, Vol. 20, No. 7, 913–926, 2006.
11. Roberts, A. R. and J. Joubert, "PML absorbing boundary condition for higher-order FDTD schemes," *Electron. Lett.*, Vol. 33, No. 1, 32–34, Jan. 1997.
12. Kantartzis, N. V. and T. D. Tsiboukis, "A higher-order FDTD technique for the implementation of enhanced dispersionless perfectly matched layers combined with efficient absorbing boundary conditions," *IEEE Transactions on Magnetics*, Vol. 34, No. 5, 2736–2739, Sept. 1998.
13. Fang, J., "Time domain finite difference computation for Maxwell's equations," Ph.D. dissertation, University of California at Berkeley, Berkeley, CA, 1989.
14. Hadi, M. F. and M. Piket-May, "A modified FDTD (2,4) scheme for modeling electrically large structures with high-phase accuracy," *IEEE Trans. Antennas Propagat.*, Vol. 45, No. 2, 254–264, Feb. 1997.
15. Hadi, M. F. and R. K. Dib, "Phase-matching the hybrid m24/s22 fdtd algorithm," in *23rd International Review of Progress in Applied Computational Electromagnetics*, 463–469, Verona, Italy, Mar. 2007.
16. Holland, R., L. Simpson, and K. Kunz, "Finite-difference analysis of EMP coupling to lossy dielectric structures," *IEEE Trans. Electromagn. Compat.*, Vol. EMC-22, No. 3, 203–209, Aug. 1980.
17. Taflove, A., *Computational Electrodynamics: The Finite-Difference Time-Domain Method*, Artech House, Boston, MA, 1995.
18. Hadi, M. F. and R. K. Dib, "Phase-matching the hybrid FV24/S22 fdtd algorithm," *Progress In Electromagnetics Research*, PIER 72, 307–323, 2007.